Nanoscale

Accepted Manuscript

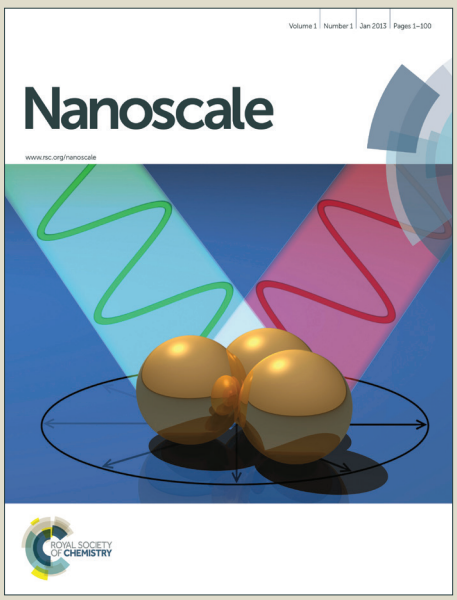

ROYAL SOCIETY OF CHEMISTRY

www.rsc.org/nanoscale

Nanoscale

RSCPublishing

PAPER

Fluidic Switching in Nanochannels for Control of Inchworm: A Synthetic Biomolecular Motor with a Power Stroke

Cite this: DOI: 10.1039/x0xx00000x

Received 00th August 2014,
Accepted 00th xx 20xx

DOI: 10.1039/x0xx00000x

www.rsc.org/

Cassandra S. Niman,[a,b] Martin J. Zuckermann,[c] Martina Balaz,[a,b] Jonas O. Tegenfeldt,[a,b] Paul M. G. Curmi,[d,e] Nancy R. Forde,[c] Heiner Linke[a,b]

Synthetic molecular motors typically take nanometer-scale steps through rectification of thermal motion. Here we propose *Inchworm*, a DNA-based motor that employs a pronounced power stroke to take micrometer-scale steps on a time scale of seconds, and we design, fabricate, and analyze the nanofluidic device needed to operate the motor. Inchworm is a kbp-long, double-stranded DNA confined inside a nanochannel in a stretched configuration. Motor stepping is achieved through externally controlled changes in salt concentration (changing the DNA's extension), coordinated with ligand-gated binding of the DNA's ends to the functionalized nanochannel surface. Brownian dynamics simulations predict that Inchworm's stall force is determined by its entropic spring constant and is ~ 0.1 pN. Operation of the motor requires periodic cycling of four different buffers surrounding the DNA inside a nanochannel, while keeping hydrodynamic load force on the DNA constant. We present a two-layer fluidic device incorporating 100 nm-radius nanochannels that are connected through a few-nm-wide slit to a microfluidic system used for *in-situ* buffer exchanges, either diffusionally (zero flow) or with controlled hydrodynamic flow. Combining experiment with finite-element modeling, we demonstrate the device's key performance features and experimentally establish achievable Inchworm stepping times on the order of seconds or faster.

Introduction

Molecular motors in living cells are multi-subunit protein assemblies that operate fundamentally differently from man-made, macroscopic machines. First, because of their small size, they are subject to thermal fluctuations in potential and kinetic energy that are comparable to the energy turnover per cycle. Second, they convert chemical energy directly into mechanical energy, omitting heat as an intermediate energy form. They are thought to use chemical energy in a cyclic process that rectifies thermal motion in an effective free-energy landscape that may contain "downhill" stretches in space, sometimes referred to as power strokes.[1,2]

The construction of synthetic molecular motors allows the study of the operational mechanisms of molecular motors in a controlled environment. A large number of approaches to synthetic motors or molecular-motor elements (such as switches and levers) have been realized, most based on small, synthetic organic molecules [3–6] or on DNA, exploiting the highly programmable nature of base-pair (bp) interactions. [7–13] This includes a highly advanced synthetic, free-running motor based on single-stranded DNA.[14] Recently, synthetic-motor concepts based protein and peptide modules have also been proposed [15,16] in an attempt to closer approximate natural protein motors.

Essentially all existing synthetic motors function entirely diffusively in the sense that motor stepping is achieved by rectification of random, thermal motion. For example, DNA motors step by diffusing from one binding site to another, biased by different affinities to binding sites [7,8,17] , but in the absence of a long-range force that would direct the motor from one binding site to the next. For motors that step by diffusion, the step size is inherently limited to the order of tens of nanometers.

Here, we propose a concept for a molecular motor, similar to that introduced in [18,19], that incorporates a pronounced power stroke that enables very large steps (~ micrometer scale) on a time scale of seconds with a finite stall force (0.1 pN). In this study we demonstrate and analyze the nanofluidic device needed to implement this motor. We name the proposed motor concept *Inchworm*. Inchworm (IW) is based on a several kbp-long, double-stranded DNA molecule confined into a nanochannel (NC) in an extended, quasi-linear conformation (Figure 1).[20–23] A power stroke can be realized by changing the salt concentration in the NC, controlling the DNA's persistence length by altering the electrostatic repulsion along its

backbone, and effectively changing the length of the DNA molecule's configuration.[24–26] We propose to induce inchworm-like stepping motion by coordinating periodic DNA length changes with cyclical binding and unbinding of the DNA ends to the NC walls using external control of IW's chemical environment. As shown below, enabled by the large extensional changes achievable in DNA, the power-stroke-driven steps of IW could be as large as a micrometer, much larger than the typical nanometer-scale step size of natural and synthetic molecular motors. Furthermore, we predict a stall force on the order of 0.1 pN, implying the ability to do work on the order of 100 pN·nm or tens of k_BT per step, a very large number compared to what can be expected for existing diffusively driven artificial molecular motors [27–29], and at least comparable to biological motors with a typical work output of $10k_BT$ per step.[2]

In the following, we introduce the IW concept in more detail. We then use Brownian dynamics simulations to characterize its stepping cycle, including its performance under a load force, and establish in this way the experimental conditions necessary to study IW performance. A key requirement to realize IW is a novel, advanced micro- and nanofluidic system for the simultaneous control of the chemical environment and, independently, the hydrodynamic flow in a NC. We describe the design and construction of a double-layer micro- and nano-fluidic device, and we demonstrate in experiment and by comparison to finite-element simulations that it fulfils the requirements for the study of IW. These results demonstrate that the IW is experimentally feasible and form the basis for the future realization of the IW motor. Furthermore, the novel nanofluidic device demonstrated here, which allows the *in-situ*, temporal control of the chemical environment in a nanoscale volume in the absence of hydrodynamic forces, holds high promise to enable novel functionalities in a wide range of other single-molecule experiments, as we will discuss below.

Inchworm Concept

Figure 1 illustrates the IW concept. It consists of a double-stranded DNA molecule, confined into a NC in a quasi-linear configuration, such that it has defined front and rear ends. Each end is functionalized with a specific sequence (*A'* & *B'*, respectively, in Figure 1) that are known to each bind to specific repressor proteins (proteins *A* and *B*, respectively, in Figure 1) in the presence of a specific ligand (*a* and *b*, respectively),[30,31] such that binding and unbinding of each IW end can be externally controlled by ligand supply. Repressor proteins *A* and *B* are bound in random spatial distribution along the inner walls of the NC.

DNA elongation and contraction can be controlled by changes in the ionic strength, induced by changes in salt concentration, of the fluid surrounding the DNA in the NC: at high salt, the negative electrostatic charges of the DNA backbone are screened, the DNA's persistence length is short, and the DNA is in a contracted state; at low salt, the backbone charges are not screened and repel each other, leading to a longer persistence length and elongated DNA.[24]

To operate IW, the buffer surrounding the motor must be cycled through a sequence of four states I –IV (Figure 1), characterized by the presence of ligand (*a* or *b*), as well as either high or low salt concentration, denoted in the following by [ligand; high/low salt]. In state I, [*a*+*b*; low salt], the salt concentration in the buffer is low (elongated DNA), and the motor is initially bound at both the *A'* and *B'* ends, due to the presence of ligands *a* and *b*. We define the motor's initial center of mass position (x_{COM}), indicated as a red dot in Figure 1 as x_0. In state II, [*b*; high salt], the DNA's *A'* end is unbound, the DNA remains bound at *B'*, and the increased salt concentration causes the DNA to contract, involving a shift in x_{COM} to position x_{II}.

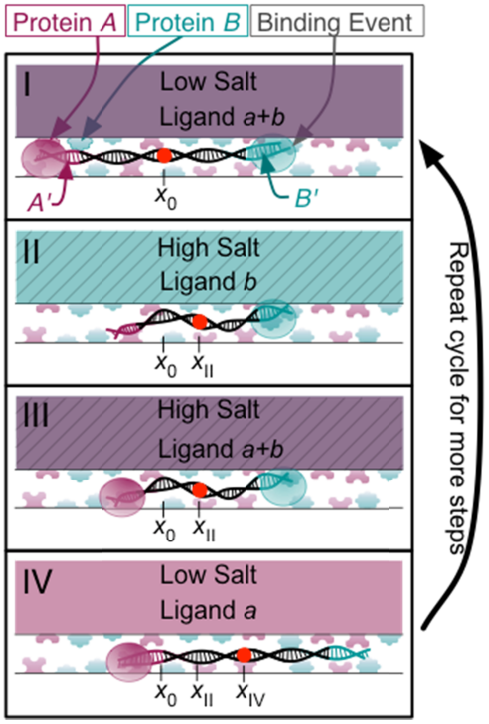

Figure 1. The Inchworm motor concept made of double-stranded DNA end sequences *A'* and *B'*, which bind to protein *A* and protein *B* in the presence of ligand *a* and ligand *b*, respectively. The DNA is in a linear conformation due to radial confinement in a nanochannel. Specific, binding of DNA ends to proteins *A* or *B*, randomly located on the channel walls, is gated by the surrounding ligands. Using external fluidic control, the DNA's chemical environment is cycled through four states I–IV, differing in the DNA length (controlled by salt concentration) and binding state (binding is indicated by a circle around the DNA end). For example, in state I the DNA is surrounded by a low salt concentration and ligands *a* and *b*, causing the DNA to be elongated, with both ends bound to proteins on the channel walls. In state II, the DNA is contracted (due to high salt concentration), and only the front sequence *B'* is bound (by presence of *b),* and so on (see also main text). To illustrate motion, the location of the DNA's center of mass (x_{COM}) is indicated by a red dot. Each full cycle of the four buffers causes the x_{COM} to progress by a distance of x_{IV}-x_0.

In state III, [a+b; high salt] the *A'* and *B'* sequences are bound. In state IV, [a; low salt] the DNA elongates while remaining bound at the *A'* end, leading to another shift in x_{COM} to position x_{IV}. Cycling through states I-IV leads to repeated steps in the same direction, each step $\Delta x_{COM} = x_{IV} - x_0$ in length. By reversing the order (I-II-III-IV versus IV-III-II-I), IW's direction of motion can be externally controlled.

Results and Discussion

Motor Model and Mechanism

Brownian dynamics simulations show that the IW concept is feasible and reveal requirements to test IW performance experimentally. To simulate IW, we use a model based on the self-avoiding walk (SAW) approach, with $N = 81$ monomers, yielding a polymer with a contour length of $L = (N-1)l_B$, where $l_B = 100$ nm is the polymer bond length, equal to about twice the persistence length of dsDNA (~50 nm in high salt). The Langevin method used to simulate the motion of the IW is formally identical to that used in [32]. In brief, the dynamics of the polymer parts in their fluid environment, and thus the effect of thermal (Brownian) motion, were modeled using the overdamped Langevin equation, which includes a stochastic, thermal force term, and neglects inertial motion (see supplementary information for details).

To model the effect of the NC, the IW polymer is confined in a hard-wall cylinder of diameter d, forcing the IW to assume a quasi-linear configuration (Figure 2 A). IW's effective length is determined in the model by a bending energy potential V_Θ, which controls the range of accessible angles between neighboring polymer bonds. When $V_\Theta = 0$, the polymer is in a freely-jointed chain (FJC) configuration. As V_Θ is increased (enforcing a straighter conformation between neighboring bonds, and simulating the effect of charge repulsion), the polymer becomes more elongated along the NC. Thus, $V_\Theta = 0$ corresponds to high salt (screened backbone charges, contracted DNA), and a finite V_Θ corresponds to low salt (elongated DNA) (Figure 2 A). The specific parameter values used in this model are provided in the supplementary information (Table S1).

The effect of thermal motion results in fluctuations in the effective length of the confined polymer, as shown in Figure 2 C (top panel) for state II and state IV. On average, the DNA has a length of 6.41 μm ± 0.16 μm in state II (contracted, high salt, $V_\Theta = 0$), and 7.10 μm ± 0.15 μm in state IV (elongated, $V_\Theta = 82$ pN·nm). Thus, its extension changes by about 9% of its total contour length with the parameters used in this simulation, and IW demonstrates an average step size of 0.7 μm.

To allow the model IW to bind to the NC walls, binding sites representing repressor proteins *A* and *B* are randomly distributed on a square lattice of lattice constant $b_R = 8$ nm placed on the wall of the cylindrical NC with 50 % of the sites vacant resulting in 7800 binding sites per square micron. Binding sites are modeled by localized potentials that can be activated or de-activated to model the presence or absence, respectively, of the corresponding ligand in the buffer. Binding is initiated when the appropriate end of the DNA diffuses within 3.45 nm of an activated binding site. The DNA unbinds when the binding site is de-activated to model a ligand exchange in the buffer. These results do not account for the DNA-protein binding kinetics, and spontaneous unbinding and re-binding will likely reduce IW performance. To reduce this a number of experimental parameters can be tuned, for example the addition of repeated binding sites at each end of the DNA, to improve experimental performance.

Successful stepping of the model IW is shown in Figure 2 B, which shows the position of the front end of the polymer upon repeated cycling through states I – IV (each full cycle lasts 0.12 s). The front end fluctuates when it is not bound (state IV), is stationary when it is bound, and steps upon change in salt concentration while unbound (transition III –IV in Figure 1). The variation in step size is about 0.12 μm and is consistent with thermal fluctuations in the DNA extension, which are about 0.15 μm. When a larger d is used, the polymer explores more space in the radial direction, reducing the elongation in the axial direction, and the step size is decreased. When changes in salt concentration are omitted from the model (only protein-binding interactions are present without changes in V_Θ) then, as expected, directional stepping ceases and the polymer effectively diffuses.

We next investigated IW's ability to operate against a load force, arising for example from an applied flow in the nanochannel. To simulate this, a rearward force, F_M, was imposed on each monomer in the direction parallel to the NC, such that the total force on the motor is given by $F_R = N F_M$. With increasing load force, the motor's step size becomes first smaller and then eventually negative, reversing motor direction (Figure 2 D). This process can be understood as the result of the competition between the polymer contraction and elongation expected due to changes in ionic strength on the one hand, and the flow-force-driven extension and contraction in state II and state IV, respectively, on the other hand. This is clearly seen in Figure 2 C where the top panel (zero load force) and bottom panel (maximum load force) show how at high load force, DNA is *shorter* in state IV, at low salt, than in state II at high salt, opposite to the salt-induced length differences under no load. At stall force (zero average step size) the distribution of DNA lengths is the same in state II and state IV (Figure 2 C, center panel). To reiterate, IW stall results from the balancing of salt-driven extension/contraction of the polymer and the counteracting flow driven contraction/extension in the nanochannel. In other words, IW's stall force is given by the externally imposed compressive (extensive) flow force which exactly compensates the salt-driven extensional (compressive) force.

Based on this consideration, we can relate the expected stall force to the polymer's, effective, entropic spring constant κ: From the thermal fluctuations of the DNA length, $\sigma_{th} \approx 0.16$ μm (from Figure 2 C top panel), one can use the equipartition theorem ($\kappa = k_B T/\sigma_{th}^2$)[23] to estimate, for the model, $\kappa \approx 0.16$ pN μm^{-1} for $N = 81$ (contour length of 8 μm).

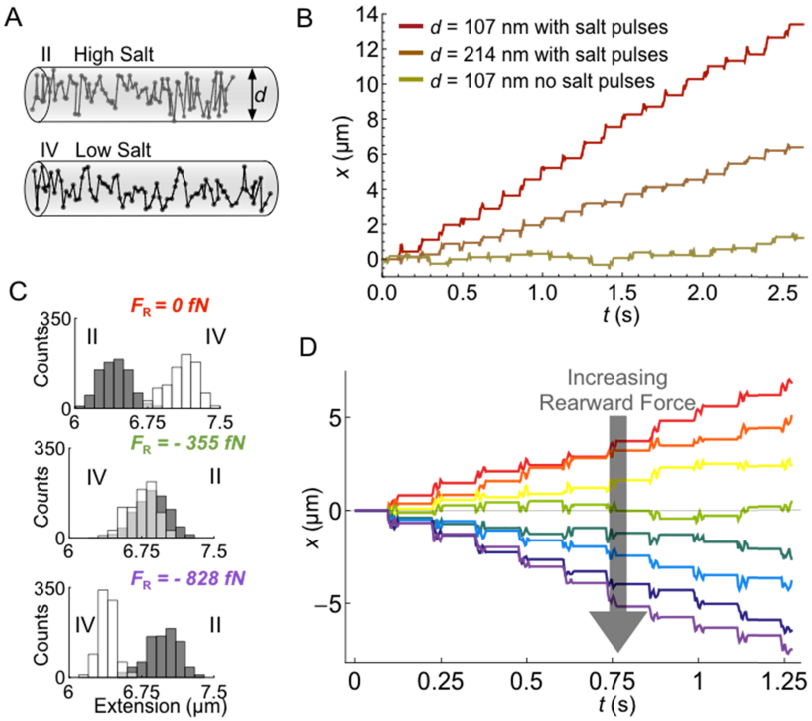

Figure 2. Brownian dynamics simulations results. (A) Snapshots of the self-avoiding walk (SAW) polymer model (monomer positions indicated as dots) confined inside a cylindrical nanochannel, 7.27 μm x 107 nm (2D projection of 3D chain, not to scale). The contracted (top) and elongated (bottom) correspond to state II (high salt, V_Θ = 0) and state IV (low salt, V_Θ turned on, see main text) in Figure 1, respectively. (B) Position *x* of the front end of the polymer versus time upon cyclical changing of buffer conditions in the model (a full cycle takes 1.8 s in the model). The top traces (red and brown) show progress for two different nanochannel widths, 107 nm and 214 nm, respectively. For the bottom trace, (yellow), changes in the coupling constant V_Θ were omitted in the model (only ligands were changed). (C) Histograms of the modeled DNA extension in states II (dark grey) and IV (light grey) with three different external forces acting on the DNA as indicated. (D) Position of the DNA front vs. time for load forces ranging from F_R= 0 fN (Red) to F_R = -828 fN (Purple), being increased by steps of 118 fN. C and D indicate a stall force of about 0.4 pN.

Assuming that stall occurs for an external force that eliminates the salt-induced length changes of ΔL = 0.7 μm in the model, we find an estimated stall force of about 0.23 pN (see supplemental information), comparable to the actual value of $F_R \approx 0.36$ pN that we find for the stall force from explicit modeling (see Figure 2 D). The remaining discrepancy may be explained by the fact that we used, in our estimate, a constant spring constant, whereas the thermal fluctuations in Figure 1 C indicate that the DNA becomes stiffer under compression in state IV. A stiffer DNA would lead to a larger stall force and better agreement between estimated and observed stall force in the model. We conclude that DNA spring constant can be used to approximately estimate IW stall force.

Implications of the Motor Mechanism for Experimental Design

This modeled contraction/elongation of DNA is well within the range that is accessible by experiment. By comparing to experimental results of DNA length in NCs at different ionic strengths [24], and rescaling with respect to contour length, we can establish that our model with its two V_Θ values approximately corresponds to a high salt of 30 mM and low salt of 1.3 mM. Thus, our modeled contraction/elongation corresponds to changes in ionic strength smaller than the range where it is reasonable to expect that proteins will remain soluble and folded over the entire salt range, between 5 mM and 500 mM. Or, put differently, the approximately 0.7 μm contraction shown in Figure 2 A and Figure 2 C (top panel) corresponds to just below 10% of the 8 μm contour length of a freely jointed chain with N = 81 monomers. Using the full range from 5 mM to 500 mM we would expect a change of 2.4 μm, about 30% of the contour length.[24] It is also important to consider that the salt-induced elongation and contraction forces must not exceed the DNA-protein binding forces. The former can be tuned by changing the range and time scales over which salt concentrations are changed, resulting in changes in stepping size and speed, while the latter could be increased, for example, with the addition of repeating binding sites at each end of the DNA. Thus, there will be considerable room to adjust experimental parameters to the needs of the involved proteins while still achieving μm-scale IW steps.

Modeling showed that it is possible to estimate IW's stall force from the DNA's effective entropic spring constant, κ, which scales inversely with contour length, L, and depends on

ionic strength and NC diameter, d.[23] Using experimentally measured thermal fluctuations of lambda DNA (contour length of 22 μm) in a 100 nm channel (but for different ionic strength than used in the model)[23], we estimate $\kappa \approx 0.01$ pN μm^{-1} (see above). Rescaling based on the contour length alone; this predicts $\kappa \approx 0.03$ pN μm^{-1} for DNA with 8 μm contour length, or about five times less stiff (lower entropic spring constant per monomer) than our modeled DNA. Thus, compared to the $F_R \approx 0.4$ pN observed for the stall force in our model (Figure 2 C, D), we expect a lower value by about a factor of five for experiment. However, this is a simplified comparison, and does not take into account the dependence of the spring constant on the DNA-excluded volume and effective persistence length, which change with the ionic strength in solution.[23]

We can conclude that an estimated stall force of order $F_{stall} = 0.1$ pN is reasonable for IW. With step size of order $\Delta x_{COM} = 1$ μm, the work done per step, $F_{stall} \Delta x_{COM} \sim 100$ pN·nm $\approx 25 k_B T$, is within the range of biological motors, which typically achieve $10 k_B T$ per step.[33] A shorter DNA with a correspondingly larger spring constant would have a larger F_{stall} but also a smaller Δx_{COM}, and we thus expect an approximately contour-length-independent work output.

Device

Device Design

Based on the modeling results above and their comparison to existing experiments, we establish the following requirements for a nanofluidic device to control and characterize IW: the device needs to provide for (i) NCs of 100–200 nm diameter to confine the DNA in quasi-linear conformation [20–25]; (ii) the ability to switch the DNA's chemical environment (buffer) in a specific, cyclical order [34,35]; (iii) the ability to minimize or apply a defined, constant load force on the DNA (crucially, this means that buffer switching must be possible without use of hydrodynamic flow in the NCs), (iv) the ability to functionalize the NC's inner walls for ligand-gated DNA binding, and (v) the capability to monitor IW in real time using epifluorescence microscopy. Importantly, such a device with the capability to independently control chemical environment and load force, combined with fluoresence microscopy, will be more generally useful for a wide range of single-molecule studies.

Figure 3 gives an overview of the device we have developed to solve this challenge. We use a two-layered design. The bottom layer consists of a set of parallel NCs (300 μm-long half cylinders with radius 100 nm) that start and end at microfluidic side channels (Figure 3 A). The side channels are used to load the NCs with DNA, and for control of pressure along the NCs. The top layer (layout is shown in Figure 3 C) is a micofluidic system that runs on top of and orthogonal to the NCs, and that allows for cyclical fluid switching of the four needed buffer solutions. A key innovation is the design of the NCs with a very narrow (5-15 nm) top opening [34] that diffusionally connects the NCs to the center microfluidic channel above, allowing for switching ligands and salt via diffusion, in the absence of flow along the NCs.

The NCs are made in optically transparent, fused silica, enabling epifluorescence imaging of the DNA from below, and allowing the use of common techniques for coating the inside of NCs with proteins or lipid bilayers.[36,37]

The microfluidic top-layer is designed for switching between four fluids in arbitrary time sequence and works as follows (Figure 3 D). [34] There is an inlet/outlet pair for each of the four buffers to minimize diffusive mixing between switching events in the microfluidics. All four inlets are kept at a pressure above the outlets. To insert a specific fluid into the center channel one applies the highest pressure to that inlet relative to the other inlets. Fluids can be switched on a time scale of 0.1–1 s.[34]

In order to be able to control the pressure drop along each NC, the device allows us to flow buffer through the side channels at the same time as through the center channels, for example to establish the same longitudinal pressure drops along center and side channels, eliminating any pressure drop along each NC. To simplify this, side channels and center channel are designed to have the same lateral dimensions and hydrodynamic resistance in the region where the nanochannels are connected.

This device is designed to be operated in one of two modes, the *force-free mode* or the *constant-force mode*. In the force-free mode, where no hydrodynamic force is to be applied to the DNA, the DNA is to be positioned inside an NC underneath the main channel of the microfluidic top layer, and is connected to the main channel diffusionally through the NC's very thin top slits, as illustrated in Figure 4 F. Finite element modeling, performed in COMSOL Multiphysics [38], shows that the concentration of small molecules equilibrates vertically between NC and microchannel within milliseconds, and that the maximum velocity in the NC induced by the constant fluid flow above the top slit is many orders of magnitude less than this average fluid flow speed (see supplementary information on modeling details). The fluid switching time (and thus the maximal IW stepping time) in this mode is then determined by the microfluidics (on the order of seconds, see above and [34]).

In the constant-force mode, a constant hydrodynamic force is applied to the IW DNA while switching among states I-IV. To achieve this, the DNA is to be positioned in a NC in the area between the main channel and a side channel, as is illustrated in Figure 4 E, and a constant flow is applied to the NC once the DNA is bound to the NC wall. We used finite element modeling to establish the required pressures to be applied to the main and side channels to yield a given hydrodynamic flow in the NCs (see supplementary information for details). The pressure gradient in the micofluidic channels is illustrated in Figure S2 B for both force-free mode, where the pressure drop along the center and side channels is equal in the region of the NCs, and constant-force mode, where the side channels are held at a lower pressure relative to the center

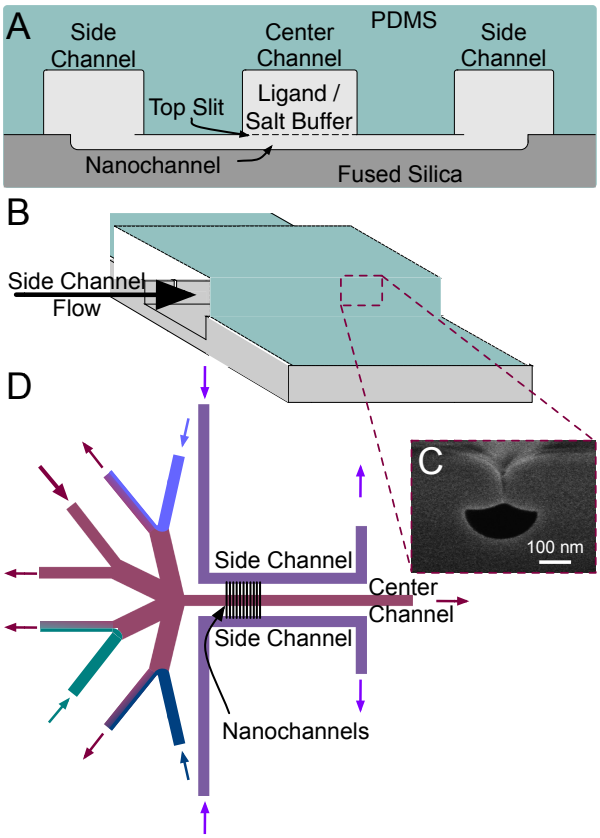

Figure 3. Two-layered fluidic device design. (A) Cross section along one nanochannel etched in fused silica. Three microfluidic channels defined in PDMS are bonded on top of the fused silica device. The side channels connect to large side openings on the nanochannels. The center channel in the PDMS is where ligand/salt buffers are exchanged over a topslit opening to the nanochannels. (B) Oblique pictorial of the device, showing the nanochannel connection to the side channel. (C) Scanning electron micrograph showing a cross section of a nanochannel coated with 7 nm metal to reduce charging effects. (D) Top view schematic of the microfluidic device made in PDMS. The side channels (purple) are used for loading the proteins and DNA into the nanochannels (black lines). The center channel has four inlet/outlet pairs for switching between the four buffers. In the situation shown, the pink fluid has the highest relative pressure on the inlet. The arrows indicate the direction of the flow.

channel. Based on the Brownian dynamics model above, we estimate that the IW can tolerate a load force of order 0.1 pN. We use this estimate to establish the required flow speed v_{stall} in the NCs: assuming a drag force per monomer of $\gamma = 1.3 \cdot 10^{-10}$ kg s^{-1} (Table S1) [39,40] and $N = 81$ monomers, we estimate $v_{stall} \approx F_{stall}/N\gamma = 10$ µm s^{-1}. NC flow speeds slower (larger) than this should lead to forward (rearward) IW motion.

Device Experimental Characterization

In the following we use a combination of experiment and analytic theory to demonstrate the key functionalities of our device. We focus on the achievable switching performance in

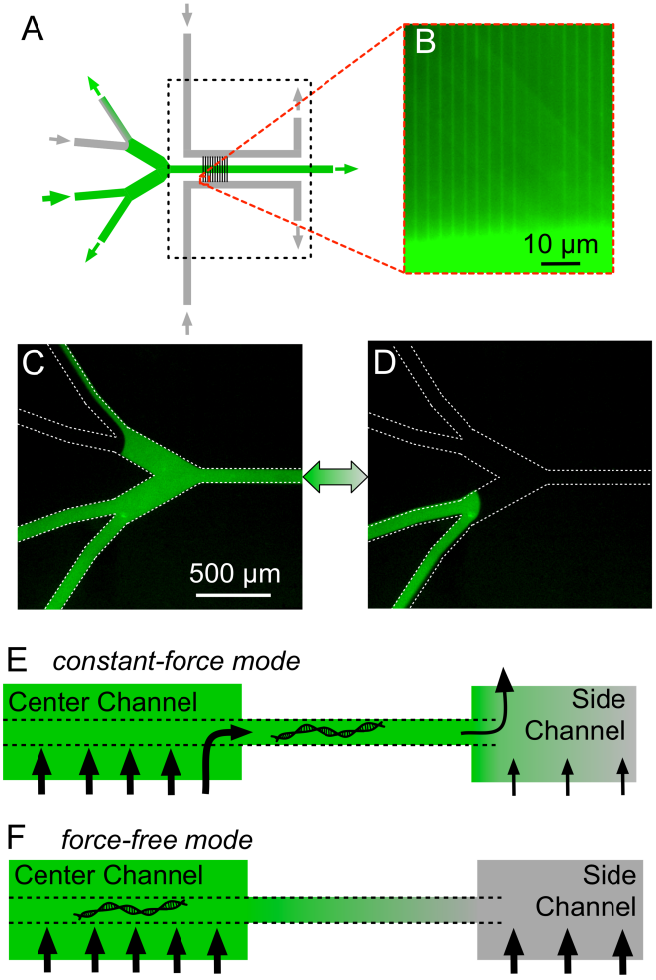

Figure 4 (A) Schematic of the device used for characterizing the fluid switching in the nanochannels, with two inlet/outlet pairs, one with water and one with fluorescent fluid. (B) Fluorescence image of the nanochannels filled with the fluorescent fluid connected to the microfluidic side channel in the bottom. (C, D) Epifluorescence images of the fluidic device in two fluidic pressure configurations (distinguished by whether the higher pressure is applied to the bottom or the top pair's inlet, respectively), filling the main channel with either clear water or fluorescein in water. (E, F) The intended location of the DNA for different measurement modes: under the main channel for force-free measurements, or to the side if a drag force is to be applied by pressure difference between main and side channels. The arrows indicate the direction of fluid flow.

the NCs, in terms of switching speed and the achievable dynamic range of concentration modulations, and we determine the experimentally achievable flow speed in the NCs, needed to control load forces. To visualize fluid switching we use fluorescein as a test solute, to represent the ligands and salt exchanges for IW.

For the characterization experiments we use a simplified microfluidic design with two inlet/outlet pairs (Figure 4 A), which we use for MilliQ water and 0.45 M fluorescein in

MilliQ water. Epifluorescence microscopy images taken with two different pressure configurations show the main channel filled with (Figure 4 C) or without (Figure 4 D) fluorescein, demonstrating fluid switching in the main channels (MilliQ water was used in the side channels). These images are in excellent qualitative agreement with those obtained by finite element simulations (see supplemental Figure S2).

Using the microfluidic control in the main channel, we established the ability to switch the fluid in the NCs from clear buffer to fluorescein buffer (Figure 4 B). It was only possible to image the fluorescent switching far from the center channel due to the high intensity of the fluid in the center channel needed to obtain a signal from the small volume of fluid in the NCs.

To characterize the time dependence of switching, we measured the fluorescence intensity in a 10 µm x 10 µm region (containing 5 NCs) located 112.5 µm from the center of the NCs, and divided this by background measured at the same distance from the main channel, but outside the NCs (Figure 5). We used a switching time of 60 s between buffer changes, and controlled the pressure drop Δp along the NCs by adjusting the flow in the side channels relative to that in the main channel, achieving switching both for an intended $\Delta p = 0$ (Figure 5 A) and for finite Δp (Figure 5 B).

The fluorescein exchange in the NC for $\Delta p = 0$ is expected to be by diffusion only, and should thus be slower than for finite Δp where both flow and diffusion contribute. Indeed, we find that the time t_s to switch the fluorescence intensity from 80 % to 20 % is longer for $\Delta p = 0$ (7.26 s ± 2.35 s) compared to finite $\Delta p = 12$ mbar (t_s = 3.23 s ± 0.59 s). The t_s data for $\Delta p = 0$ across the NCs is somewhat noisy due to the practical limitation on the switching of the fluid via diffusion far form the center channel.

Analysis

To further analyze the switching behaviour shown in Figure 5 we used analytic approaches. (finite element simulations to analyze the fluid behavior far from the center channel were not feasible due to the large aspect ratio of the NCs). Our goal was to predict the achievable speed and dynamic range of concentration switches as a function of position in the NCs. To do so, we first determined the effective fluorescein diffusion coefficient in the NCs (which is expected to be lower than the bulk value) from our data.

We began by determining the effective fluorescein diffusion coefficient D_{eff} in the NCs from the data taken at $\Delta p = 0$ (Figure 5 A**).** We solved Fick's 2nd law in one dimension with the appropriate initial and boundary conditions (derivations shown in supplementary material) resulting in a time-dependent concentration profile in the NCs of

$$C(x_{NC},t) = 1 - \left\{ \frac{x_{NC}}{l} + \frac{2}{\pi} \sum_{n=1}^{\infty} \frac{1}{n} \mathrm{Exp}\left[-D_{eff} t \left(\frac{n\pi}{l} \right)^2 \right] \sin\left[\frac{n\pi x_{NC}}{l} \right] \right\} \quad (1)$$

where t is time, l is the length of the NC from the center channel to the side channel, and x_{NC} is the position along the NC measured. Fitting this data with D_{eff} as the only variable, using Mathematica [41], to six intensity vs. time switching events from the experimental data, where $x_{NC} = 62.5$ µm and $l = 100$ µm, we found $D_{eff} = 3.0 \cdot 10^{-10} \pm 0.5 \cdot 10^{-10}$ m^2 s^{-1}.

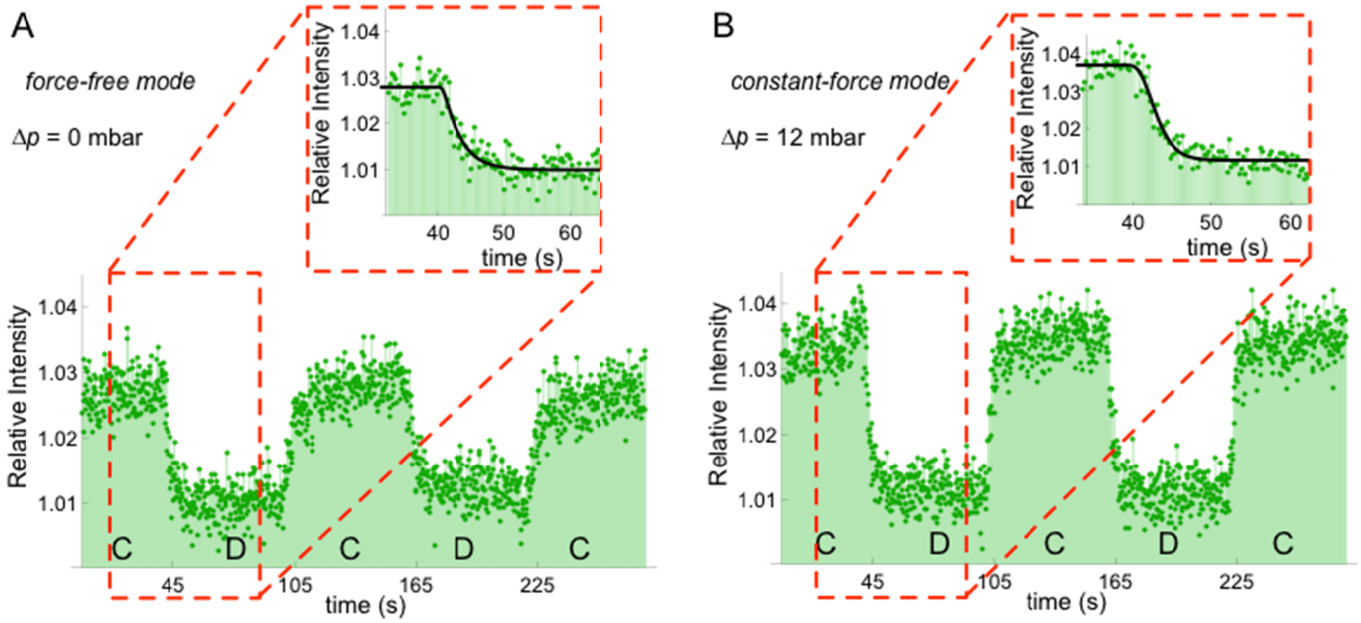

Figure 5. (A) Experimental results (extracted from epifluoresence images) when the pressure difference, Δp, across the nanochannels is 0 mbar. The relative intensity in the nanochannels vs. time when switching between state C and D shown in Figure 4. The inset shows one switching event and the theoretical fit to equation (1), the black line. (B) shows the changes in intensity vs. time when the pressure difference across the nanochannels is 12 mbar. The inset shows one switching event and, as a black line, the fit to equation (2).

This is 61 % of fluorescein's free diffusion coefficient of $4.9 \cdot 10^{-10}$ m^2 s^{-1} (calculated using the Wiley-Chang Correlation at 25 ºC in [42]). This reduced diffusion coefficient is likely due to hindrance of the particle movement due to the high concentration of particles in solution. These particle-particle interactions predict a reduction in the effective diffusion coefficient of 65 %.[43] Due to the high amount of surface area compared to volume of solution in NCs, near-wall interactions may play an additional part in the hindered diffusion seen [44], making it important to measure D_{eff}.

Using the appropriate boundary conditions of finite Δp (see supplemental information) when solving Fick's 2nd law results in a time-dependent concentration of

$$C(x_{NC},t) = 1 - \mathrm{Erf}\left[\frac{x_{NC} - vt}{2\sqrt{D_{eff}\,t}}\right] \qquad (2)$$

where v, the variable parameter in the nonlinear least squares fit, is the fluid velocity in the NC.[45] Using the D_{eff} found from the previous analysis and fitting six intensity vs. time switching events for finite Δp (Figure 5 B) we obtain a fluid velocity of $v = 20.70 \pm 2.31$ µm s^{-1} for a specific pressure setting, establishing that we can control flow speeds of the correct order (10 µm s^{-1}) to control relevant load forces on IW. Increasing the fluid velocity further is done by simply increasing the pressure to the central channel inlets.

From these theoretical models we can also map out what the switching time at any position along the NC should be for $\Delta p = 0$ or finite Δp, with a fluid velocity of 21 µm s^{-1} in the NCs. In Figure 6 we have plotted the theoretical switching time, t_s, from equation (2), for a fluid velocity in the NCs of 21 µm s^{-1}, measured experimentally in blue with diamond markers. In the $\Delta p = 0$ scenario it is impossible to attain a full concentration switch in much of the NC, due to the linear concentration gradient along the NC at equilibrium. We have therefore plotted in yellow with circle markers the time to switch between 80 % and 20 % in the local concentration, t_{sl}, as well as the switching time of global concentration, t_{sg}, in pink from equation (1). The switching times from these curves, using values from the non-linear least-squares fits of the data, are within one standard deviation from the measured switching time of the raw data. From these analytical models and the results of the finite element simulations this device fulfils all the requirements for IW and we are able to predict the switching time and fluid speed of the fluid surrounding IW anywhere in the NCs.

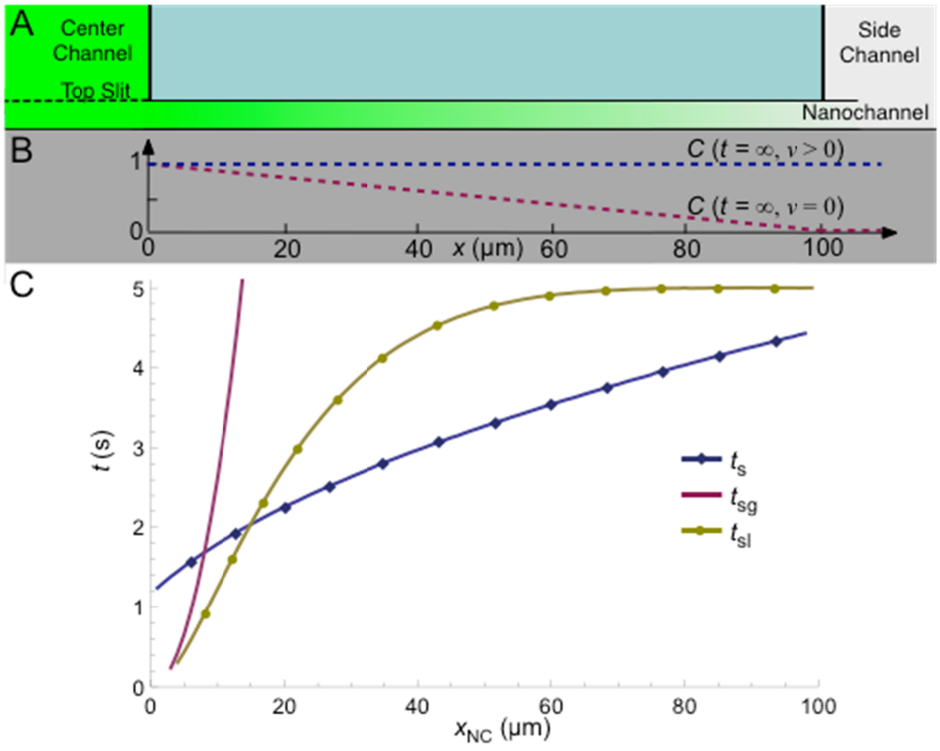

Figure 6. Analytic results on predicted fluid switching in the nanochannels. (A) Schematic of a cross section of a nanochannel. (B) Equilibrium concentration profile in the nanochannel when there is a fluid velocity $v > 0$ in dashed-blue and for $v = 0$ in dashed-pink. (C) Calculated switching as a function of position in the nanochannel ($x_{NC} = 0$ is at the edge of the center microfluidic channel as indicated). The solid pink curve, t_{sg}, is the switching time in the nanochannel when there is no fluid flow and only switching due to diffusion. This results in a linear, final equilibrium concentration profile (see B), such that concentrations cannot switch from 20% to 80% beyond 20 µm along the 100 µm channel. The solid yellow curve with circle markers, t_{sl}, is the switching time from 20% to 80% of the final concentration at equilibrium at a given length along the channel. This corresponds to the intensity we measured experimentally. The solid blue curve with diamond markers is the switching times, t_s, when the fluid in the nanochannel is moving with an average velocity of 21 µm s^{-1}.

Conclusion

We have proposed a novel concept for an artificial, biomolecular motor that utilizes a pronounced power stroke and can take repeated, micron-sized steps with an expected stepping time on the order of seconds or better. Our simulations show that the motor's stall force is of the order of 0.1 pN, corresponding to hydrodynamic drag achievable by flow speeds of tens of μm s^{-1}, or cargo transport of a micrometer-size bead at around 10 μm s^{-1}. This makes IW amenable to real-time observation of linear stepping with simultaneous characterization of its ability to do work – neither of which has been achieved to date with artificial motors. The IW concept thus can be seen as a significant step forward in synthetic-motor design.

Furthermore, we have designed, fabricated and tested a nanofluidic device, which meets all of the requirements to make and test IW. A key innovation is the use of a nanoscale topslit that connects our NCs to a separate microfluidic system. This device will permit us to not only observe DNA in NCs with different salt concentrations in real time, as has been achieved previously [25], but also to control the fluid flow at the level needed to measure force-velocity curves for IW, and even stop it, in the NCs. Furthermore, our microfluidic design allows the change between more than two solutions in arbitrary time sequence, making it possible to control both forward and rearward motion of IW. This design of a nanofluidic device is the main innovation needed to realize IW, with other essential steps (such as control of changes of DNA length in an NC with real time observation [25]) achieved previously elsewhere.

To complete the experimental realization of IW, as we have proposed it, the following needs to be done. The NCs need to be coated with randomly distributed, functional repressor proteins. We intend to use the larger opening to the NC connected to the side channels in the microfluidics to flow the proteins to the inner NC walls using external pressure. Functionalization can be achieved, for example, by linking biotinylated repressors via streptavidin to biotinylated BSA [46] or a biotinylated lipid bilayer [36]. IW DNA is then to be introduced into the NC via overpressure or electrophoresis as is commonly done.[20,24] Orientation of the DNA can be accomplished with the addition of a loading chamber, where one end of the DNA can be bound forcing the free end to enter the nanochannel first when the bound end is released. To test IW without load force, the DNA will be positioned just below the center microfluidic channel (force-free mode, Figure 4 E), keeping the side channels at an appropriate pressure to minimize flow in the NCs. Switching from state I to IV or from IV to I it should be possible to make IW walk in either direction. Because the steps predicted here are large, only a few steps are needed to verify IW movement. To test IW performance against a load force, the DNA can be moved within the NC to a position in between the center channel and side channel (constant-force mode, Figure 4 E) where we can control the fluid flow to the degree necessary (a few μm s^{-1} up to tens of μm s^{-2} or more), as we have demonstrated above.

The fluidics device presented here has many uses outside of the IW motor. For example, the ability to change solutions in a NC and observe changes in real time without inducing a drag force on the DNA can be useful for further studies of DNA, including melt mapping for genomics. [47] It is also amenable to single-molecule studies where one would like to, for example, observe protein motors moving along DNA, now without an external force acting on the protein.[34,48,49] Where protein movement is studied without external force, this device gives the ability to change chemical environment unlike standard techniques.[49,50] Furthermore, NCs of diameter ≈ 100 nm can be used to study actomyosin motility in a 3D configuration similar to that in the sarcomere (and unlike the planar configuration of traditional motility assays), as recently demonstrated in hollow nanowires.[51] Using NCs with open top slits will allow for continuous ATP supply along long channels [52,53], including the capability to turn motors on and off. Switchable motility in long NCs may also be useful for improved biocomputation devices based on motility assays, for example to introduce local, chemical gating.[54]

Experimental Section

Device Fabrication

Nanochannel fabrication

NCs were made as in [53], in quartz, 1" x 1" fused silica substrates with a thickness of 500 μm (Structure Probes Inc. Supplies, PA, USA). To clean the quartz before fabrication we rinsed the quartz in running MilliQ water for 10 min, then placed the quartz in RCA1: 70% MilliQ, 15% NH_3 (> 25% in water solution) (VWR, PA, USA), and 15% H_2O_2 (>30%) (VWR, PA, USA) heated to 70-80 ºC, adding the H_2O_2 just before the quartz was added. The quartz was then rinsed in running MilliQ water for 10 min, then placed in RCA2: 70% MilliQ water, 15% HCl (>37%) (VWR, PA, USA), and 15% H_2O_2 (>30%) heated up to 70-80 ºC, adding the H_2O_2 just before the quartz was added. The quartz was rinsed in running MilliQ water for 10 min, and then dried in N_2.

A 30 nm-thick layer of silicon was evaporated onto the quartz via thermal evaporation (Pfeiffer Classic 500L, Pfeiffer Vacuum, Asslar, Germany). About 10 nm of the silicon layer on quartz was oxidized with O_2 gas flow 1501 h^{-1} at 1000 ºC for 5 min (Rapid Thermal Process Oven 1200, UniTemp, Pfaffenhofen, Germany). Quartz was cleaned in acetone (VWR, PA, USA) then isopropanol (VWR, PA, USA) in an ultrasonic bath for 5 min each, dried in N_2 and exposed to oxygen plasma for 90 s (Plasma-Preen, Plasmonic Systems, Inc., NJ, USA).

To prepare for patterning we spin-coated with a mixture of ZEP520A7:anisol, 1:1 (Zeon Corporation, KY, USA) at 3000 rpm for 60 s and baked it on a hot place at 180 ºC for 60 s resulting in a resist layer of 110 nm. To create a conductive layer we spin-coated with Espacer 300z (Showa Denko, Tokyo, Japan) at 2000 rpm for 60 s and baked it on a hot plate at 80 ºC for 60 s resulting in a 20 nm layer of Espacer. To

pattern the NCs and loading zones we used electron beam lithography, each NC made was of 4 single-pixel lines with 8 nm between (EBL Raith 150, Raith, Dortmund, Germany). Pixel step size was set to 4 nm with a dose of 550 μC cm^{-1} at accelerating voltage of 30 kV and 7.5 μm aperture size. Loading zones were made with area dose of 250 pC cm^{-2}. To remove Espacer the quartz was rinsed in MilliQ water for 30 s. Patterns in ZEP520 were developed in hexyacetate at 0 ºC for 45 s then rinsed in IPA for 30 s and dried in N_2. Descumming was done using oxygen plasma, 10 sccm O_2, 50 mT pressure, RF power 50 W for 15 s; SiO2 was etched in 10 sccm CHF3, 50 mT pressure, and RF power 75 W for 45 s (Sirus T2 Reactive Ion Etcher, TRION Technology, AZ, USA). The Si was etched in 20 sccm Cl_2, 5 mT pressure, RF power 100 W, and ICP power of 300 W for 15 min then the substrate was cooled in 12 sccm He at 5 T pressure (ICP-RIE, Oxford Instruments, Oxford, UK). To remove remaining resist it was soaked in Remover1165 for 10 min on a hot plate at 100 ºC followed by a rinse in MilliQ water and dried in N_2. Then the substrate was exposed to oxygen plasma, both front and back side each for 3 min. The quartz was then cleaned with the initial RCA1 and RCA2 cleaning procedure.

To etch the quartz NCs we placed the quartz in buffered oxide etch 10:1 (VWR, PA, USA) for 2 min then rinsed it in running MilliQ water for 5 min and dried with N_2. Oxidation of the silicon layer to reduce top slit size was performed with dry thermal oxidation at 1100 ºC for 1 h (Omega Junior Diffusion Furnace, Tempress, Vaassen, Netherlands). Finally, we repeated the initial cleaning in RCA1 and RCA2.

Microfluidic fabrication

The microfluidic device layer was made of polydimethylsiloxane (PDMS). The mould for the microfluidic channels was made of SU8 2050 (MicroChem, MA, USA) on a silicon wafer. A silicon wafer that was baked in an oven at 200 ºC for 30 min, followed by SU8 2050 spin-coating at 500 rpm for 10 s then 2500 rpm for 60 s. Then the wafer was baked on hot plates for 3 min at 65 ºC then 10 min at 95 ºC and left at room temperature for 5 min. The SU8 was patterned with UV lithography in a contact mask aligner (Karl Süss, Muncih, Germany) at 7.5 mW cm^{-2} for 21 s. The mask design in shown in Figure 7. The wafer was then baked on hot plates for 1 min at 65 ºC, then 4 min at 95 ºC.

The wafer was developed for 5 min in the SU8 developer (MicroChem, MA, USA), rinsed in streaming isopropanol, dried in streaming N_2 gas, and baked in an oven for 30 min at 200 ºC. The resulting patter was 50 μm in height. The wafer was given an anti-sticking treatment in tridecafluoro-(1,1,2,2)-tetrahydrooctyl-trichlorosilane (FT-TCS, Sigma Aldrich, St. Louis. MO, USA) to facilitate demoulding of the PDMS.

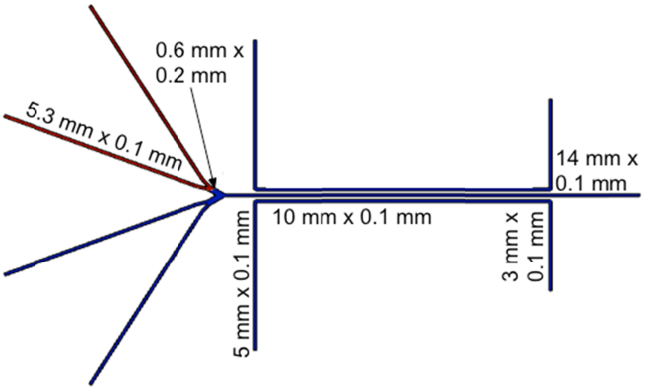

Figure 7. COMSOL simulation results illustrating the microfluidics layer dimensions. The UV mask design file, used for fabrication of the mould, was used in the COMSOL simulation shown here. The device is 50 μm in height.

The PDMS polymer base and curing agent (Sygard 184, Down Corning, Midland, MI, USA) were mixed at 10:1, degassed, poured onto the wafer, and cured in an oven for 1 h at 80 ºC. The PDMS was peeled off the wafer and holes were punched at each inlet and outlet. The 50 μm tall PDMS channel and the NC quartz piece were exposed to oxygen plasma for 30 s (Plasma Preen II-852, Plasmantic Systms, Inc, North Brunswick, NJ, USA) and then aligned and bonded together. Silicone tubes, 3 mm x 5 mm (VWR, PA, USA), were cut 10 mm long, sonicated in 2% Helmanex (VWR, PA, USA), rinsed in MilliQ water twice, dried in N_2 and then glued around the punched holes on top of the PDMS using a silicone adhesive (ElastosilA07, RTV-1 silicone rubber, Wacker Silicones, Munich, Germany).

Pressure Control

To control the pressure on the inlets of the microfluidics a Fluigent microfluidic control system (MFCS-FLEX-3C system, pressure range 0–69 mbar, Fluigent, Paris, France) was connected via a FLUIWELL-3C system with 2 ml-vials connected to the silicone tubes glued atop the PDMS device. The feedback coefficient was set to 5 to get a balance between control of the pressure and the time after switching to equilibrate, using the software provided with the Fluigent system. A script was used to automatically switch the inlet pressures in the inlets of each inlet/outlet pair between 35 mbar and 43 mbar every 60 s. The inlets on the side channels were held at a constant pressure, either 20 mbar (force-free mode), or 5 mbar (constant-force mode). The side channel inlet pressures are those found from the fluidics simulations and are discussed further in the supplementary information. All outlet tubes were used as reservoirs held at atmospheric pressure.

Imaging

In order to visualize the fluid switching one of the inlets was filled with MilliQ water and the other was filled with 0.45 M fluorescein (Life Technologies Corporations, Paisley, UK) in MilliQ water filtered using a 0.2 μm Supor® membrane

syringe filter (VWR, PA, USA). The fluorescein in the micro- and nanochannels was imaged through the bottom of the quartz substrate using an inverted Nikon Eclipse TE2000-U microscope using epifluorescence (Nikon Corporations, Tokyo, Japan) with either a 4x Plan Fluor objective or a 60x Plan Fluor water immersion objective (Nikon Corporations, Tokyo, Japan). All measurements were performed at room temperature. The detector used was an Andor iXon-EM+ camera, model DU-897D (Andor Technology, Belfast, Northern Ireland), and the light source was the Lumen 200 (Prior Scientific Inc., Rockland, MA, USA).

Fluidics Simulations

Two finite element simulations in COMSOL Multiphysics (COMSOL AB, Stockholm, Sweden) were performed to better understand the two-layer fluidic system.[38] In both simulations we used the function for "laminar flow" and "transport of a dilute species". We assume the diluted solute does not influence the viscosity or density of the fluid and this does not take into account particle-particle-hindered diffusivity. The material in the channel was set to have the viscosity and density of water. The sidewalls were defined by no-slip boundaries with no flux. Inlets were given the appropriate pressure relative to the outlets, set at 0 mbar. Some inlets were also set to have fluid entering with a solute with $D = 4.9 \cdot 10^{-10}$ m^2 s^{-1} (fluorescein).[42]

The first simulation of the microfluidic channels was done in 2D using the shallow channel approximation of 50 µm, shown in Figure 7 and Figure S2 A. The geometry was imported from the UV mask design file. The inlet pressures on the inlets of the two inlet/outlet pairs of the center channel are 47 mbar and 35 mbar, and the concentration of the solute is 0 mM and 1 mM respectively to simulate fluorescein, used experimentally. The side channels have inlet pressures of 25 mbar in one simulation and 5 mbar in the other, results in Figure S2 B show top and bottom respectively, and both have solute concentration of 0 mM. The stationary solution using "laminar flow" and "transport of a dilute species" agree with experimental observation and are further discussed in the supplementary information.

The second simulation, of a cross section of the NCs with a large microfluidic channel above, was done in 2D. The geometry of the channel is illustrated in Figure S3. For the second simulation we used a stationary solution for the "laminar flow", and a second time-dependent solution using the velocity field from the first solution as the initial conditions. The time-dependent solution was solved with both "laminar flow" as well as "transport of diluted species." The left side of the large microfluidic channel is an inlet with a pressure 0.26 mbar and solute concentration 1mM. The top boundary is set to be mirrored and the right most boundary is an outlet. Both the velocity profile of the fluid, results shown in Figure S3, and the concentration of the fluid in the channel, shown in Figure S4, are discussed further in the supplementary information.

Acknowledgements

We thank Brian Long for his contribution to the conception of the Inchworm motor. We also thank Anders Kvennefors and Mariusz Graczyk for their assistance in device fabrication, Jason Beech for contributions to the overall device design, and Henrik Persson for valuable discussions. We thank IRMACS of Simon Fraser University for the use of its computer facilities and ComputeCanada for financial support to use the Westgrid Computer Network. This work was financially supported by the Human Frontier Science Program (RGP0031/2007), the Swedish Research Council (project 2010-4527), the Nanometer Structure Consortium (nmC@LU), and an NSERC Discovery Grant.

Notes and references

[a] Division of Solid State Physics, Lund University, Box 118, 22100 Lund, Sweden
[b] Nanometer Structure Consortium (nmC@LU), Lund University, Box 118, 22100 Lund, Sweden
[c] Department of Physics, Simon Fraser University, Burnaby, British Columbia, Canada
[d] School of Physics, University of New South Wales, Australia
[e] Centre of Applied Medical Research, Australia

Electronic Supplementary Information (ESI) available: See DOI: 10.1039/b000000x/

1. J. Howard, *Curr. Biol.*, 2006, **16**, R517–9.
2. J. Howard, *Mechanics of Motor Proteins and the Cytoskeleton*, Sinauer Associates, 2001.
3. V. Balzani, A. Credi, F. Raymo, and J. Stoddart, *Artificial Molecular Machines.*, 2000, vol. 39.
4. E. R. Kay, D. A. Leigh, and F. Zerbetto, *Synthetic molecular motors and mechanical machines.*, 2007, vol. 46.
5. B. L. Feringa, *J. Org. Chem.*, 2007, 72, 6635–6652.
6. M. von Delius, E. M. Geertsema, and D. A. Leigh, *Nat. Chem.*, 2010, **2**, 96–101.
7. J. Bath and A. J. Turberfield, *Nat. Nanotechnol.*, 2007, **2**, 275–284.
8. B. Yurke and A. P. Mills, *Genet. Program. Evolvable Mach.*, 2003, **4**, 111–122.
9. J. Bath and A. J. Turberfield, 2013, **81**, 81–82.
10. W. B. Sherman and N. C. Seeman, *Nano Lett.*, 2004, **4**, 1203–1207.
11. J. S. Shin and N. A. Pierce, *J. Am. Chem. Soc.*, 2004, **126**, 10834–10835.
12. T. Omabegho, R. Sha, and N. C. Seeman, *Science*, 2009, **324**, 67–71.
13. M. You, Y. Chen, X. Zhang, H. Liu, R. Wang, K. Wang, K. R. Williams, and W. Tan, *Angew. Chemie - Int. Ed.*, 2012, **51**, 2457–2460.
14. S. F. J. Wickham, M. Endo, Y. Katsuda, K. Hidaka, J. Bath, H. Sugiyama, and A. J. Turberfield, *Nat. Nanotechnol.*, 2011, 6, 166–169.
15. E. H. Bromley, N. J. Kuwada, M. J. Zuckermann, R. Donadini, L. Samii, G. A. Blab, G. J. Gemmen, B. J. Lopez, P. M. Curmi, N. R. Forde, D. N. Woolfson, and H. Linke, *HFSP J*, 2009, **3**, 204–212.

16. M. Mickler, E. Schleiff, and T. Hugel, *ChemPhysChem*, 2008, 9, 1503–1509.
17. M. Liu, R. Hou, J. Cheng, I. Y. Loh, S. Sreelatha, J. N. Tey, J. Wei, and Z. Wang, *ACS Nano*, 2014, **8**, 1792–803.
18. Z. Wang, *Phys. Rev. E - Stat. Nonlinear, Soft Matter Phys.*, 2004, **70**.
19. D. Li, D. Fan, and Z. Wang, *J. Chem. Phys.*, 2007, **126**.
20. J. O. Tegenfeldt, C. Prinz, H. Cao, S. Chou, W. W. Reisner, R. Riehn, Y. M. Wang, E. C. Cox, J. C. Sturm, P. Silberzan, and R. H. Austin, *Proc. Natl. Acad. Sci. U. S. A.*, 2004, **101**, 10979–10983.
21. L. J. Guo, X. Cheng, and C. F. Chou, *Nano Lett.*, 2004, **4**, 69–73.
22. C. H. Reccius, J. T. Mannion, J. D. Cross, and H. G. Craighead, *Phys. Rev. Lett.*, 2005, **95**.
23. W. Reisner, J. N. Pedersen, and R. H. Austin, *Reports Prog. Phys.*, 2012, 75, 106601.
24. W. Reisner, J. P. Beech, N. B. Larsen, H. Flyvbjerg, A. Kristensen, and J. O. Tegenfeldt, *Phys. Rev. Lett.*, 2007, **99**.
25. C. Zhang, K. Jiang, F. Liu, P. S. Doyle, J. a van Kan, and J. R. C. van der Maarel, *Lab Chip*, 2013, **13**, 2821–6.
26. K. Jo, T. M. Schramm, and D. C. Schwartz, *Methods Mol. Biol.*, 2009, **544**, 29–42.
27. L. Samii, H. Linke, M. J. Zuckermann, and N. R. Forde, *Phys. Rev. E - Stat. Nonlinear, Soft Matter Phys.*, 2010, **81**, 021106.
28. L. Samii, G. A. Blab, E. H. C. Bromley, H. Linke, P. M. G. Curmi, M. J. Zuckermann, and N. R. Forde, *Phys. Rev. E - Stat. Nonlinear, Soft Matter Phys.*, 2011, **84**, 031922.
29. T. Hugel and C. Lumme, *Curr. Opin. Biotechnol.*, 2010, 21, 683–689.
30. C. L. Lawson and P. B. Sigler, *Nature*, 1988, **333**, 869–871.
31. Z. Wang, M. P. Schmitt, and R. K. Holmes, *Infect Immun*, 1994, **62**, 1600–1608.
32. N. J. Kuwada, M. J. Zuckermann, E. H. C. Bromley, R. B. Sessions, P. M. G. Curmi, N. R. Forde, D. N. Woolfson, and H. Linke, *Phys. Rev. E*, 2011, 84.
33. C. Bustamante, Y. R. Chemla, N. R. Forde, and D. Izhaky, *Annu. Rev. Biochem.*, 2004, **73**, 705–748.
34. C. S. Niman, J. P. Beech, J. O. Tegenfeldt, P. M. G. Curmi, D. N. Woolfson, N. R. Forde, and H. Linke, *Lab Chip*, 2013, **13**, 2389–96.
35. P. B. Allen, G. Milne, B. R. Doepker, and D. T. Chiu, *Lab Chip*, 2010, **10**, 727–733.
36. F. Persson, J. Fritzsche, K. U. Mir, M. Modesti, F. Westerlund, and J. O. Tegenfeldt, *Nano Lett.*, 2012, **12**, 2260–5.
37. B. Sweryda-Krawiec, H. Devaraj, G. Jacob, and J. J. Hickman, *Langmuir*, 2004, **20**, 2054–2056.
38. 2012, Version 4.3a.
39. M. Liu and J. Giddings, *Macromolecules*, 1993, 3576–3588.
40. M. T. Downton, M. J. Zuckermann, E. M. Craig, M. Plischke, and H. Linke, *Phys. Rev. E - Stat. Nonlinear, Soft Matter Phys.*, 2006, **73**.
41. 2010, Version 8.0.
42. S. A. Rani, B. Pitts, and P. S. Stewart, *Antimicrob. Agents Chemother.*, 2005, **49**, 728–732.
43. G. K. Batchelor, *J. Fluid Mech.*, 1976, 74, 1.
44. K. D. Kihm, A. Banerjee, C. K. Choi, and T. Takagi, *Exp. Fluids*, 2004, 37, 811–824.
45. H. Bruus, *Physics (College. Park. Md).*, 2008, **18**, 363.
46. Y.-H. Sen, T. Jain, C. A. Aguilar, and R. Karnik, *Lab Chip*, 2012, 12, 1094.
47. W. Reisner, N. B. Larsen, A. Silahtaroglu, A. Kristensen, N. Tommerup, J. O. Tegenfeldt, and H. Flyvbjerg, *Proc. Natl. Acad. Sci. U. S. A.*, 2010, **107**, 13294–13299.
48. B. Liu, R. J. Baskin, and S. C. Kowalczykowski, *Nature*, 2013, **500**, 482–5.
49. T. D. Silverstein, B. Gibb, and E. C. Greene, *DNA Repair (Amst).*, 2014.
50. S. M. Block, L. S. Goldstein, and B. J. Schnapp, *Nature*, 1990, **348**, 348–352.
51. M. Lard, L. Ten Siethoff, J. Generosi, A. Månsson, and H. Linke, *Nano Lett.*, 2014, **14**, 3041–6.
52. R. Bunk, M. Sundberg, A. Månsson, I. A. Nicholls, P. Omling, S. Tågerud, and L. Montelius, *Nanotechnology*, 2005, 16, 710–717.
53. M. Graczyk, M. Balaz, A. Kvennefors, H. Linke, and I. Maximov, *J. Vac. Sci. Technol. B Microelectron. Nanom. Struct.*, 2012, **30**, 06FF09.
54. D. V. Nicolau, G. Solana, K. L. Hanson, L. Filipponi, L. Wang, and A. P. Lee, *Microelectron. Eng.*, 2006, **83**, 1582–1588.

